12th International Symposium on Turbulence and Shear Flow Phenomena (TSFP12)
Osaka, Japan, July 19–22, 2022

ON THE ROLE OF THE KELVIN-HELMHOLTZ WAVE OF TURBULENT FLOWS OVER PERMEABLE POROUS WALL

Yusuke Kuwata
Department of Mechanical Engineering,
Osaka Prefecture University
Sakai, Osaka 599-8531, Japan.
kuwata@me.osakafu-u.ac.jp

ABSTRACT

Direct numerical simulations (DNSs) of porous-walled channel flows with computational domain size constraints were performed to clarify the role of large-scale turbulent motions associated with the Kelvin–Helmholtz (K–H) instability on turbulent flows over porous walls. The constraints of the domain size was imposed to control the large-scale motions, enabling us to discuss the isolated roles of the near-wall turbulent motions and large-scale motion. In addition, we considered thick and thin porous walls to isolate the effects of roughness and permeability. It is found that near-wall turbulent motions, including streaks and longitudinal vortices, are predominantly altered by the surface roughness rather than the wall permeability, whereas the wall permeability is essential for the development of the large-scale motions. The large-scale motion, which is organized into spanwise rollers, contributes to an increase in turbulent friction drag, and induces the large-scale streamwise perturbation near the thick porous wall. Discussions in the logarithmic mean velocity profile based on the Jackson model confirms that the large-scale motion increases the von Kármán constant, which is considered to reflect an increase in the characteristic vortex size due to the large-scale motions.

Introduction

A turbulent flow around a porous wall is of special interest in engineering because of considerable heat and mass transfer performance due to larger specific surface area. As the surface roughness and wall permeability of porous media have a large impact on turbulent flows over porous media, particular attention is paid to control turbulent boundary layer by modification of porous walls characteristics. It is well established that porous media usually increases turbulence and momentum exchanges across the porous/fluid interface (Suga *et al.*, 2010), whereas the drag reduction is sometimes achieved by streamwise-preferential porous walls (Gómez-de Segura & García-Mayoral, 2019). The distinctive features of the porous wall turbulence is the presence of the large-scale motions associated with the K–H instability (Kuwata & Suga, 2016*b*, 2017). However, the turbulent flows over porous walls consists of near-wall streaks and longitudinal vortices with a superimposition of large-scale motions, and the coexistence of fine-scale and large-scale motions makes it difficult to identify the role of the large-scale motion. The goal of this study is to clarify how roughness and permeability alter turbulent flows over porous walls and identify the role of large-scale motion associated with the K–H instability.

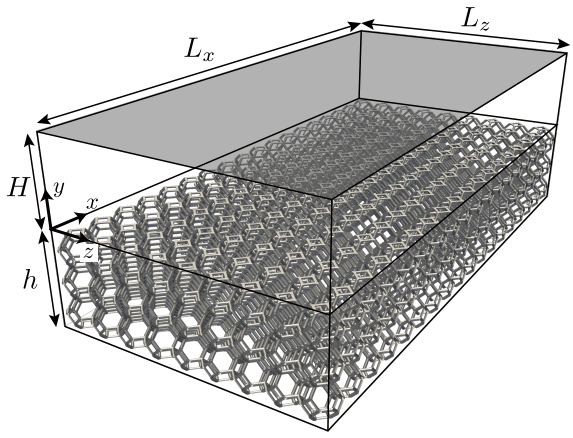

Figure 1. Flow configuration of a porous-walled channel flow.

Flow conditions

The configuration of a porous-walled channel flow is presented in Figure 1, where H and h are the channel and porous wall heights, respectively. We considered a solid wall for the top and bottom walls at $y = H$ and $y = -h$, respectively, whereas a porous wall was considered in lower part of the channel $-h < y < 0$. The flow was periodic in the streamwise (x) and spanwise (z) directions, and the flow was driven by a mean streamwise pressure gradient. The highly isotropic permeable porous media of the porosity $\varphi = 0.95$ was modeled as arrays of Kelvin cells (Thomson, 1887). The size of the single unit of the Kelvin cell was set to $L = H/3$, and the resulting permeability was $K/H^2 = 6.4 \times 10^{-4}$. In this study, to discuss isolated effects of surface roughness and wall permeability, we considered two porous walls: one was the case with sufficiently thick porous wall of $h = H$, and the other was the case with thin porous wall of $h = H/3$.

As for the computational domain size, the computational domain of $L_x(x) \times (H+h)(y) \times L_z(z)$ with $L_x = 6H$ and $L_z = 3H$ was considered for the baseline case as in Kuwata & Suga (2016*b*, 2017). In addition to the baseline case, we performed simulations with the streamwise-reduced domain of $L_x = H$ and the spanwise-reduced domain of $L_z = H$, both of which was designed such that the domain was large enough to sustain near-wall turbulent vortices but was too small to prop-

erly reproduce the streamwise perturbations modulated by the spanwise rollers. As the streamwise length of $L_x = H$ is shorter than the wavelength of the streamwise perturbations, the streamwise-reduced domain does not accommodate the spanwise rollers. In contrast, the spanwise rollers are enhanced by the spanwise-reduced domain because the coherence of the spanwise rollers is reinforced by the spanwise periodical conditions with insufficient spanwise separation. We considered six simulation cases with different computational domain sizes and porous wall heights, as shown in Figure 2. In the following, for the sake of brevity, cases were named according to AxBz-C, where $A = L_x/H$ is the streamwise domain length, $B = L_z/H$ is the spanwise domain length, and C is either "thin" ($h = H/3$) or "thick" ($h = H$), as shown in Fig.2.

The numerical method for the present DNS study is the lattice Boltzmann method (LBM). Owing to the high efficiency of massive parallel computing and easiness of handling complex geometry, the LBM is highly suited to DNS of turbulent flows over resolved porous walls (Kuwata & Suga, 2016*b*, 2017; Kuwata *et al.*, 2020). There are several possible choices for the LBM models, the D3Q27 multiple-relaxation-time LBM (Suga *et al.*, 2015) was used, which has been extensively validated against canonical flows and successfully applied to turbulent flows over porous and rough walls (Kuwata & Suga, 2016*b*, 2017; Kuwata *et al.*, 2020; Kuwata & Nagura, 2020). As the LBM is discretized with uniform spacing grid, exceedingly fine grid that satisfies the near-wall resolution requirement should be used throughout the computational domain. This requires a large investment of computer resources for the DNSs. To circumvent the the computational demands, we applied the local grid refinement proposed by Kuwata & Suga (2016*a*). The grid resolution near the porous wall was determined such that the grid spacing in wall units are less than 2.0 wall units as in the previous lattice Boltzmann DNS studies (Kuwata & Suga, 2016*b*, 2017; Kuwata *et al.*, 2020; Kuwata & Nagura, 2020), and the resulting total number of grid points for the baseline case of 6x3z-thick is approximately 800 millions. In this resolution, the single unit of the Kelvin cell was resolved by 101 grid points along each direction. The grid independence test confirmed that further refinement of the grid resolution by a factor of 1.5 yielded a change in the skin friction coefficient by 0.4%.

Results and discussions

Figure 3 shows snapshots of the streamwise velocity fluctuations above the porous wall at $y^{p+} \simeq 10$ where $y^{p+} = yu_\tau^p/\nu$ is the inner-scaled distance from the porous wall with u_τ^p being the friction velocity at the porous wall. For the streamwise-reduced cases (1x3z), near wall turbulence is sustained for the thick and thin porous wall cases, and we observe no distinct difference in turbulent vortex structure between the thin and thick wall cases. For the spanwise-reduced cases (6x1z), a clear difference is detectable between the thin and thick wall cases; turbulence structure for the thick porous wall case is characterized by streamwise alternating low- and high-speed regions, whereas no such streamwise perturbation is observed from the thin porous wall case. This streamwise perturbation is similar to what has been reported in the DNS of porous wall turbulence by Kuwata & Suga (2016*b*, 2017), who concluded that the streamwise perturbation was the footprint of the spanwise rollers associated with the K–H instability. For the full-domain cases (6x3z), the streamwise alternating low- and high-speed regions for 6x3z-thick are rather obscure than those for 6x1z-thick, whereas turbulence structure over the thick

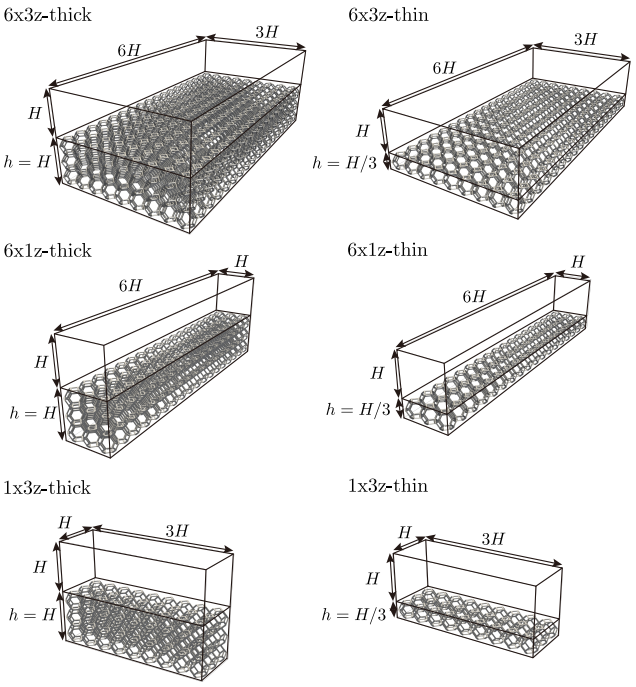

Figure 2. Computational domain for all simulation cases.

porous wall seems to be different from that over the thin porous wall. For case 6x3z-thick, the turbulent structure is characterized by the relatively larger high- and low-speed regions which have a connection in the spanwise direction rather than in the streamwise direction. The first look of the snapshots of the velocity fluctuations confirms that the spanwise rollers associated with the K-H instability develops for the baseline case of 6x3z-thick and spanwise-reduced domain case of 6x1z-thick, and the coherence of the spanwise rollers is more significant for the case 6x1z-thick.

The presence of the large-scale motion can be quantitatively detectable from the one-dimensional streamwise premultiplied energy spectra of streamwise velocity fluctuations at $y^{p+} \simeq 10$ as shown in Figure 4. It is evident from Fig.4 (a,b) that the energy spectra for cases 6x3z-thick and 6x1z-thick exhibit a pronounced peak around $\lambda_x/\delta_p = 3-5$. Here, δ_p denotes the boundary layer thickness over the porous wall, which is defined as the distance from $y = 0$ to the position at the zero-total shear stress. Since the wavelength of $\lambda_x/\delta_p = 3-5$ roughly corresponds to the characteristic wavelength of the K–H instability (Kuwata & Suga, 2017; Suga *et al.*, 2018), we can conclude that the relatively large-scale turbulence structures as observed for cases 6x1z-thick and 6x3z-thick in Fig.3 is attributed to the K–H instability. Another noticeable observation from the figure is that, for the streamwise-reduced domain cases (1x3z) in Fig.4(c), the energy spectra for the thin and thick porous wall cases perfectly collapse onto each other. For the streamwise-reduced domain cases (1x3z), the streamwise length is long enough to sustain near-wall turbulence including the streaks and longitudinal vortices but too short to accommodate the spanwise rollers. Given that only the near-wall turbulence develops for cases 1x3z, we can assert that near-wall turbulence is unaffected by the thickness of the porous wall. In other words, the near-wall turbulence is predominantly altered by the surface roughness rather than the wall permeability.

To better understand the effect of the large-scale motion on mean flow properties, Figure 5 depicts streamwise mean velocity profiles normalized by the friction velocity. For com-

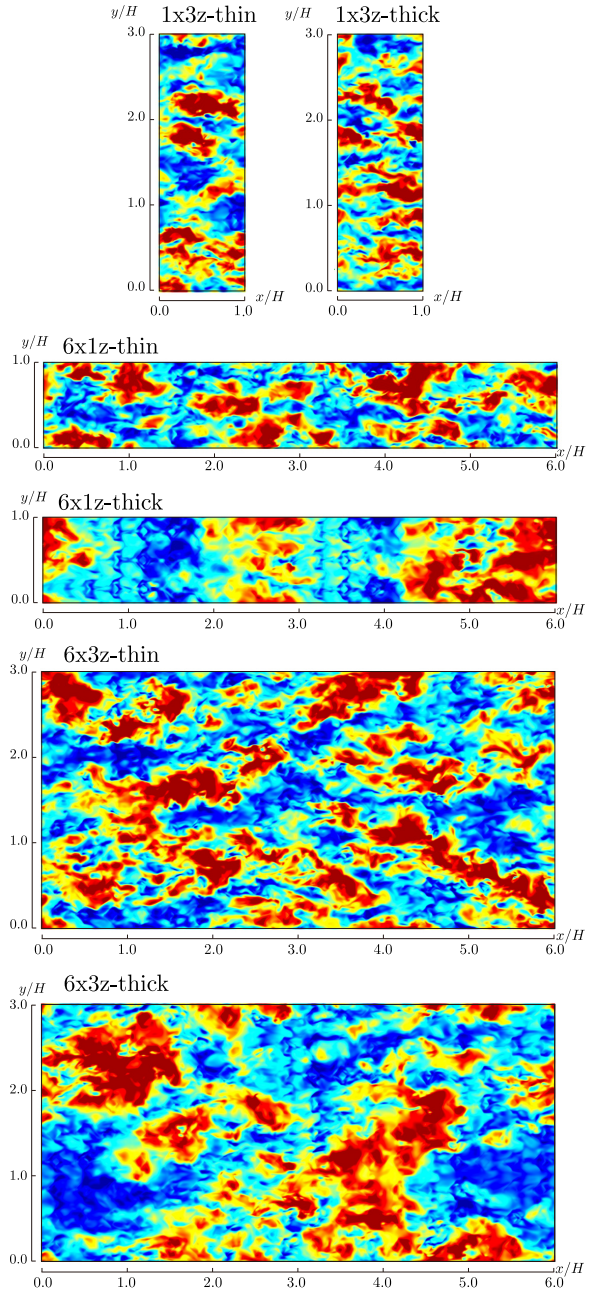

Figure 3. Snapshots of streamwise velocity fluctuations just above the porous wall at $y^{p+} \simeq 10$.

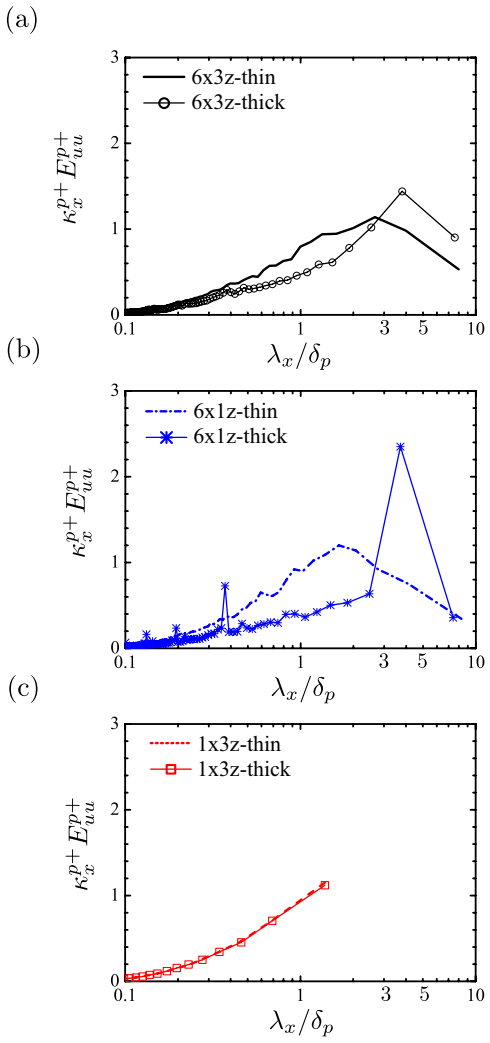

Figure 4. Pre-multiplied one-dimensional streamwise spectra just above the porous wall at $y^{p+} \simeq 10$: (a) for cases 6x3z, (b) for cases 6x1z, and (c) for cases 1x3z.

parison, DNS data for smooth wall turbulence at $Re_\tau = 590$ by Vreman & Kuerten (2014) is also included. As the porous wall increases the friction drag, the mean velocity profile exhibits significant asymmetry, and the profile is lower than that of the smooth wall result. For the streamwise-reduced domain cases (1x3z) in Fig.5(c), no visible difference in the mean velocity profile is detectable between the thin and thick porous wall cases. In contrast, for the full-domain cases (6x3z) in Fig.5(a) and the spanwise-reduced cases (6x1z) in Fig.5(b), the profile over the thick porous wall is considerably lower than that over the thin porous wall. The possible explanation for this trend is responsible for the spanwise rollers, which develop for the thick wall cases but not for the thin wall cases, as observed in Fig.3. For the full domain cases of 6x3z, the skin friction coefficient at the thin porous wall is 5.7 times larger than the smooth wall result from Vreman & Kuerten (2014), and it is further increased by 43% for the thick porous wall case. This suggests that the friction drag at the porous wall is increased not only by the surface roughness but also by the spanwise rollers associated with the K-H instability. .

The effects of the domain size and porous wall thickness on turbulence intensity are presented in Figures 6 and 7 where the streamwise component and wall-normal component normalized by the friction velocity at the porous walls are shown. For comparison, the DNS data for a smooth wall at $Re_\tau = 590$ from Vreman & KuertenVreman & Kuerten (2014) are included.

For the thin porous walls in Figs.6(a) and 7(a), the maximum peak just above the porous wall is absent, while the strength of the wall-normal component is maintained. This trend is similar to what has been found for the rough wall turbulent boundary layer Ligrani & Moffat (1986); Flack *et al.* (2005); Kuwata & Kawaguchi (2019). Regarding the effects of the domain size, the profiles near the thin porous walls are insensitive to the domain size. For the thick porous walls in Figs.6(b) and 7(b), the modification of the Reynolds stress appears qualitatively similar to thin porous wall cases, while the domain size has a substantial influence on the turbulence intensity unlike the thin porous wall cases. Inside the porous wall ($y < 0$), the turbulence intensity are the largest for the spanwise-reduced domain case (6x1z), followed by the full-

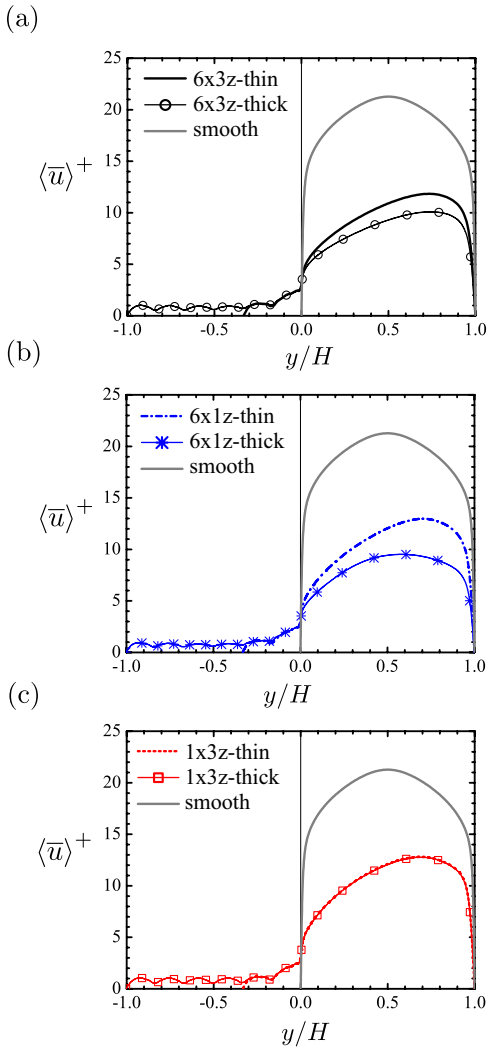

Figure 5. Comparison of the inner-scaled mean velocity profile: (a) for cases 6x3z, (b) for cases 6x1z, and (c) for cases 1x3z.

domain case (6x3z), and the smallest for the streamwise-reduced domain case (1x3z). Over the thick porous wall, the increased wall-normal component and decreased streamwise component are more prominent for the 6x1z-thick where the strong spanwise rollers are artificially induced by the periodic conditions with an insufficient separation. Hence, it is suggested that the spanwise rollers increases the wall-normal Reynolds stress while decreasing the streamwise component.

Finally, we discuss the effect of the spanwise rollers on the logarithmic mean velocity profile. The logarithmic velocity profile for turbulent flows over a porous wall is customary written as follows:

$$U^{p+} = \frac{1}{\kappa}\ln\left(\frac{y+d}{h_r}\right), \tag{1}$$

where U^{p+} is the mean velocity normalized by the friction velocity at the porous wall, and the parameters κ, d, and h_r are the von Kármán constant, zero-plane displacement, and equivalent roughness height, respectively. There are several possible routes for determining those parameters. One of the widely-used approach in the field of porous wall turbulence is fitting the mean velocity profile to the logarithmic law of Eq.1, where

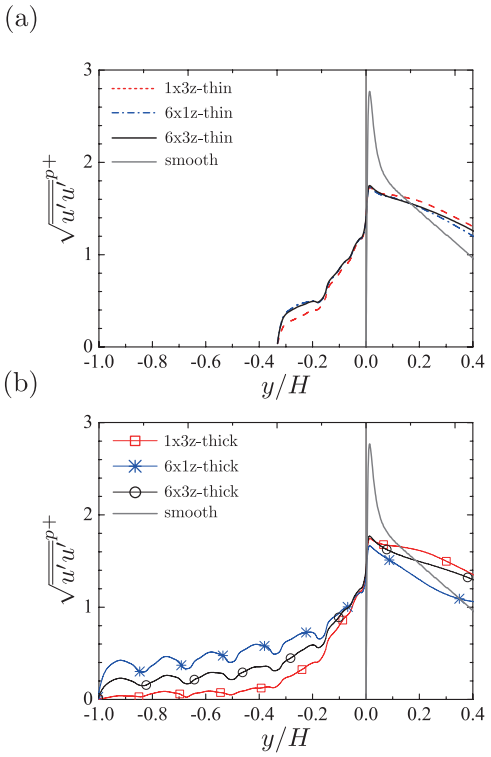

Figure 6. Streamwise turbulence intensity normalized by the friction velocity at the porous wall: (a) thin porous wall cases and (b) thick porous wall cases.

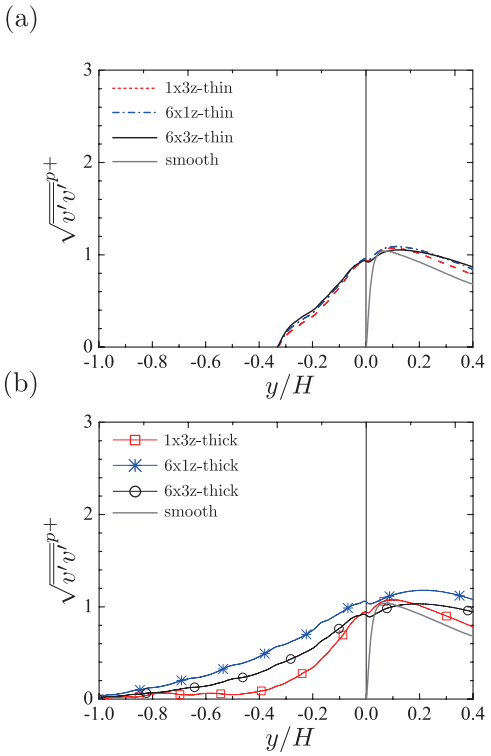

Figure 7. Wall-normal turbulence intensity normalized by the friction velocity at the porous wall: (a) thin porous wall cases and (b) thick porous wall cases

the zero-plane displacement d is first determined based on the diagnostic function γ:

$$\gamma = (y+d)^{p+}\frac{dU^{p+}}{dy^{p+}}. \tag{2}$$

The value of d is determined such that the diagnostic function γ takes plateau in the logarithmic region. The von Kármán constant κ is given as the inverse of the plateau value of γ (i.e., $\kappa = 1/\gamma$), and the equivalent roughness height is obtained by fitting Eq.(1) to the mean velocity profile. Another well-known approach to obtain the value of d is using the Jackson model Jackson (1981). In this approach, d is assumed to be the level at which the height-averaged drag force acts:

$$d_J = \frac{\int_{-h}^{0} y f_x dy}{\int_{-h}^{0} f_x dy}. \tag{3}$$

where f_x is the x-z plane-averaged drag force. Since this approach does not assume the logarithmic velocity profile of Eq.(1), it is particularly useful for relatively low Reynolds number flows where the logarithmic region is not guaranteed. Figure 8 presents the diagnostic function with the zero-plane displacement obtained by the Jackson model Jackson (1981). The DNS result for the smooth wall case at $Re_\tau = 590$ from Vreman & Kuerten (2014) is shown for comparison. Note that the results for the reduced domain cases of 6x1z and 1z3z are not shown here because the logarithmic mean velocity profiles cannot be properly represented by the reduced domain cases. We see that the diagnostic function γ for smooth wall case does not take a plateau in the logarithmic region because the Reynolds number under consideration is not so sufficiently high that the mean velocity profiles follows the logarithmic law. This implies that fitting to the log-law profile of Eq.(1) yield unphysical log-law parameters of κ, d, and h_r. The figure shows that for the porous wall cases, the diagnostic function for the thick wall case in Fig.8(a) is shifted downward with respect to the smooth wall result, while that for the thin wall case in Fig.8(b) is close to the smooth wall result. Given that the plateau value of the diagnostic function corresponds to inverse of the von Kármán constant, the observation suggests that the von Kármán constant for the thin porous wall case is almost the same as that for the smooth wall case, while that for the thick porous wall case takes a somewhat larger value.

The logarithmic velocity profiles with the log-law parameters by the fitting approach and Jackson model are compared in Figure 9. The zero-plane displacement by the fitting approach d_{fit}^{p+} is larger than that by the Jackson model d_{mJ}^{p+}, and the corresponding von Kármán constant is considerably lower than the standard value of $\kappa = 0.41$. We observe that the mean velocity profiles with the scaling of $(y+d_{fit})^{p+}$ perfectly follows the log-law profile with a considerably steeper slope in comparison with the smooth wall case. It should be however remarked that the low-law parameters obtained by the fitting approach do not have any physical implications because those parameters are simply the results of overfitting of the low-Reynolds number results to the log-law profile. Concerning the profiles with d_{mJ}, although the agreement is not perfect, the profile over the thin porous wall can be reasonably approximated by the log-law profile with $\kappa = 0.41$, whereas a somewhat larger value of $\kappa = 0.49$ offers a good approximation for the velocity profile over the thick porous wall.

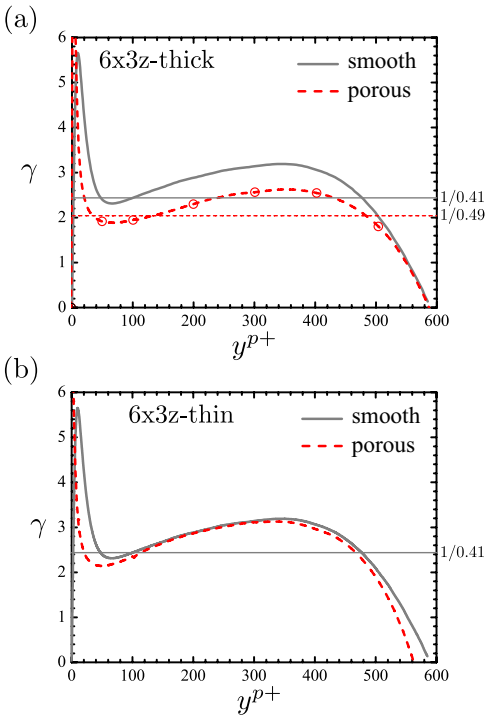

Figure 8. Comparison of the diagnostic function γ with the zero-plane displacement by the Jackson model: (a) thin porous wall cases and (b) thick porous wall cases. The DNS result for the smooth wall case at $Re_\tau = 590$ from Vreman & Kuerten (2014) is shown for comparison.

The larger value of κ for the thick porous wall case is physically interpreted as the results of the spanwise rollers. It has been well established that the vortex size is directly related to Prandtl's classical mixing length, which scales with the distance from the wall with the proportional constant of κ. In the context of the turbulence over the thick porous wall, turbulent motions consist of the near-wall turbulent motion with a superimposition of the spanwise rollers; thus, the characteristic vortex size for the thick porous wall appears to be larger than that for the thin porous wall, as observed in Fig.3. The increase in the vortex size by the spanwise rollers means an increase in the mixing length, implying an increase in the proportional constant of the mixing length κ from the standard value of 0.41. Slight deviation for the log-law profile is due to the low-Reynolds number effect as can be seen in the profile of γ in Fig.8. It is conceivable that an increase in the von Kármán constant for the thick porous wall case is the result of an increase in the characteristic vortex size due to the presence of the large-scale motion. Indeed, although the results are not shown here, the mixing-length for the thick porous wall is larger than that for the thin porous wall case, and the increased mixing-length for the thick porous wall case can be reasonable represented by the classical mixing-length model with the increased von Kármán constant.

Conclusions

The influence of spanwise rollers associated with K–H instability on a turbulent flow over a porous wall was systematically studied using DNSs of porous-walled channel flows with constraints in the size of the computational domain. We performed the simulations with the truncated domains, which were large enough to sustain the near-wall turbulence includ-

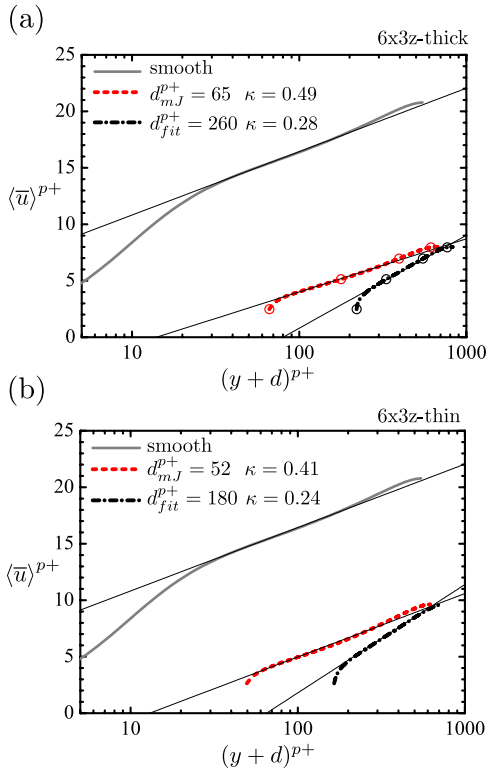

Figure 9. Inner-scaled mean velocity profile with the logarithmic scaling: (a) thin porous wall cases and (b) thick porous wall cases. The scaling with the fitting approach $(y+d_{fit})^{p+}$ and Jackson model $(y+d_{mJ})^{p+}$ are shown. For comparison, the DNS result for the smooth wall case at $Re_\tau = 590$ from Vreman & Kuerten (2014) is included.

ing the streaks and longitudinal vortices but too small to properly capture spanwise rollers by the K-H instability. For each domain case, we considered thick and thin porous walls for the bottom wall. The thin porous wall effectively attenuates the effect of wall permeability, maintaining the effect of the surface roughness. The constrained DNSs aims to clarify how surface roughness and wall permeability alter turbulent flows over porous walls and identify the role of the spanwise rollers associated with the K–H instability.

A turbulent flow over a porous wall consists of near-wall turbulent motions with a superimposition of the spanwise rollers owing to the K–H instability. The near-wall turbulent motions are found to be insensitive to the thickness of a porous wall, and a modification of the the near-wall turbulent motions by a porous wall is principally due to the role of the surface roughness of a porous wall. The spanwise rollers with streamwise alternating low- and high-speed regions develop over the thick porous wall and contribute to an enhancement of the turbulence inside a porous wall, leading to an increase in the skin friction coefficient at a porous wall. Hence, wall permeability plays an important role in sustaining the spanwise rollers but not in modification of the near-wall turbulent motions.

To discuss the mean flow away from a porous wall, we discuss the logarithmic scaling of the mean velocity profiles with two commonly used definitions of zero-plane displacement. The fitting approach, in which the zero-plane displacement is obtained by fitting the mean velocity profile to the logarithmic law, yields a considerably smaller von Kármán constant, irrespective of the presence of spanwise rollers. For the scaling with the Jackson mode, the von Kármán constant for a thin porous wall is the same as that for a smooth wall, while that for the thick porous wall case is increased by 20% for the standard value. The increased von Kármán constant for the thick porous wall case is considered to reflect an increase in the characteristic vortex size owing to the spanwise rollers. The relatively large-scale spanwise rollers, which dominate turbulent motions for the thick porous wall cases, increase the characteristic vortex size, i.e., the mixing length, leading to an increase in the von Kármán constant.

REFERENCES

Flack, Karen A, Schultz, Michael P & Shapiro, Thomas A 2005 Experimental support for townsend ' s reynolds number similarity hypothesis on rough walls. *Phys. Fluids* **17** (3), 035102.

Jackson, PS 1981 On the displacement height in the logarithmic velocity profile. *J. Fluid Mech.* **111**, 15–25.

Kuwata, Y. & Kawaguchi, Y. 2019 Direct numerical simulation of turbulence over systematically varied irregular rough surfaces. *J. Fluid Mech.* **862**, 781–815.

Kuwata, Y. & Nagura, R. 2020 Direct numerical simulation on the effects of surface slope and skewness on rough-wall turbulence. *Phys. Fluids* **32** (10), 105113.

Kuwata, Y. & Suga, K. 2016*a* Imbalance-correction grid-refinement method for lattice Boltzmann flow simulations. *J. Comput. Phys.* **311**, 348–362.

Kuwata, Y & Suga, K 2016*b* Lattice Boltzmann direct numerical simulation of interface turbulence over porous and rough walls. *Int. J. Heat Fluid Flow* **61**, 145–157.

Kuwata, Y. & Suga, K. 2017 Direct numerical simulation of turbulence over anisotropic porous media. *J. Fluid Mech.* **831**, 41–71.

Kuwata, Y., Tsuda, K. & Suga, K. 2020 Direct numerical simulation of turbulent conjugate heat transfer in a porous-walled duct flow. *J. Fluid Mech.* **904**.

Ligrani, P. M. & Moffat, R. J. 1986 Structure of transitionally rough and fully rough turbulent boundary layers. *J. Fluid Mech.* **162**, 69–98.

Gómez-de Segura, G. & García-Mayoral, R. 2019 Turbulent drag reduction by anisotropic permeable substrates–analysis and direct numerical simulations. *J. Fluid Mech.* **875**, 124–172.

Suga, K., Kuwata, Y., Takashima, K. & Chikasue, R. 2015 A D3Q27 multiple-relaxation-time lattice Boltzmann method for turbulent flows. *Comput. Math. Appl.* **69**, 518–529.

Suga, K., Matsumura, Y., Ashitaka, Y., Tominaga, S. & Kaneda, M. 2010 Effects of wall permeability on turbulence. *Int. J. Heat Fluid Flow* **31**, 974–984.

Suga, K., Okazaki, Y., HO, U. & Kuwata, Y. 2018 Anisotropic wall permeability effects on turbulent channel flows. *J. Fluid Mech.* **855**, 983–1016.

Thomson, William 1887 Lxiii. on the division of space with minimum partitional area. *The London, Edinburgh, and Dublin Philosophical Magazine and Journal of Science* **24** (151), 503–514.

Vreman, A.W. & Kuerten, J.G.M. 2014 Statistics of spatial derivatives of velocity and pressure in turbulent channel flow. *Phys. Fluids* **26** (8), 085103.